RSC Advances

RSC Publishing

PAPER

View Article Online
View Journal | View Issue

Fabrication of hierarchical flower-like super-structures consisting of porous $NiCo_2O_4$ nanosheets and their electrochemical and magnetic properties

Cite this: *RSC Advances*, 2013, **3**, 4372

Zhao-Qing Liu,[a] Kang Xiao,[a] Qi-Zhi Xu,[a] Nan Li,[a] Yu-Zhi Su,*[a] Hong-Juan Wang[a] and Shuang Chen*[b]

Received 28th November 2012,
Accepted 21st January 2013

DOI: 10.1039/c3ra23084h

www.rsc.org/advances

In the present work, we demonstrate a facile and cost-effective strategy for synthesizing hierarchical flower-like super-structures consisting of porous $NiCo_2O_4$ nanosheets. The morphologies and surface areas of $NiCo_2O_4$ samples can be tailored by changing the reaction time. The synthesized $NiCo_2O_4$ samples are characterized by scanning electron microscopy (SEM), transmission electron microscopy (TEM), powder X-ray diffraction (XRD), Raman spectroscopy, X-ray photoelectron spectroscopy (XPS), and by using an accelerated surface area and porosimetry analyzer (ASAP 2020M). The $NiCo_2O_4$ samples exhibit high activity and superior cycling stabilities in ORR. In addition, the magnetic properties of $NiCo_2O_4$ samples are also studied in detail.

1. Introduction

Recently, nanostructured materials have attracted extensive interest from the materials community because of their special properties and wide applications. The morphologies of nanostructures that determine the surface arrangements and coordinations may exert great influence on the corresponding performances.[1,2] Accordingly, the design and synthesis of nanostructured materials with controlled shapes and sizes have stimulated considerable research efforts in seeking novel morphology-dependent physical properties and functions.[3,4] As one of the typical nanostructures, two-dimensional (2D) nanosheets or nanoplates have attracted tremendous attention due to the pronounced quantum surface effects and dramatic changes in electronic structures.[5] 2D nanosheets can bridge the gap between the quantum world of one-dimensional nanomaterials and three-dimensional nanomaterials. In particular, the development of transitional metal oxide nanosheets has been intensively pursued on the basis of fundamental scientific interest coupled with the wide potential for many technological applications.[6]

The hierarchical assembly of nanoscale building blocks into superstructures or complex architecture has attracted extensive interest.[7] Among the various surface morphologies, the hierarchical superstructure is an important complex morphology, and it can be made up by building nanoscale units at different levels with the higher control levels.[8] The hierarchical assembly of nanoscale building units into a superstructure represents a significant challenge in the field of nanomaterial science and is a crucial step to realize functional nanodevices. Furthermore, the hierarchical superstructure can offer a large number of fundamental scientific opportunities for studying the effects of dimensionality and size with respect to their collective optical, magnetic, and electronic properties and would provide possibilities to study the novel performances and applications resulting from the arrangement of the nanoscale units and spatial orientation.[9] Accordingly, the fabrication of a hierarchical superstructure consisting of nanosheets may open new possibilities for wide applications in future nanodevices. Herein, hierarchical flower-like nanosheet super-structures are pursued.

$NiCo_2O_4$ is an interesting binary oxide with applications in many fields, such as flat panel displays,[10] ferrofluid technology,[11] electrocatalysis,[12] drug delivery and hyperthermia,[13] photodetectors,[14] chemical sensors,[15] *etc.* Up to now, various $NiCo_2O_4$ morphologies, such as nanoplates,[16] mesoporous structures,[17,18] nanoparticles,[19] nanoneedles[20] and nanowires,[21] have been prepared through various routes including hydroxide decomposition, thermal treatment, hydrothermal synthesis, and so on. However, to our knowledge, in only a few of these studies have the morphologies and nanostructures of $NiCo_2O_4$ been systematically investigated, let alone the relationship between the nanostructure and the corresponding physicochemical properties. In this work, we demonstrate the fabrication of hierarchical flower-like super-structures consisting of porous $NiCo_2O_4$ nanosheets and present their electrochemical and magnetic properties. In addition to the merits of superstructures and nanosheets, the porous structures will be

[a]*School of Chemistry and Chemical Engineering, Guangzhou University, Guangzhou 510006, China. E-mail: lzqgzu@gzhu.edu.cn; syzbox@yahoo.com.cn*
[b]*Guangzhou institute of railway technology, Guangzhou 510430, China. E-mail: drschen@126.com; Fax: +86-20-39366908; Tel: +86-20-39366908*

preferable for the following reasons: (*i*) as electrode material, the porous nanosheets with large specific surface area and porous configuration can greatly improve the electrode/electrolyte contact area, shorten the diffusion path of current carriers. (*ii*) The conductivity of porous nanomaterials can be easily enhanced by doping metal nanoparticles with high conductivity into the pores, and the doped metal nanoparticles will serve as an intervening ''spacer'' matrix for electron transmission. The hierarchical flower-like superstructures consisting of porous $NiCo_2O_4$ nanosheets will enable greater control of the material morphology and performance on the nanometer scale, which will find potential applications in electrochemical devices, magnetic devices, gas sensors, carriers, and in other fields.

2. Experimental section

Materials synthesis

All the reagents used in the experiment were of analytical grade and were used without further purification. In a typical procedure, 0.02 mol of urea was dissolved in 20 mL deionized water under constant stirring, followed by the addition of 1 mmol $Ni(NO_3)_2{\cdot}6H_2O$ and 2 mmol $Co(NO_3)_2{\cdot}6H_2O$. The mixture was stirred for 30 min, the transparent solution was transferred to a Teflon-lined autoclave (25 mL capacity). The hydrothermal process was conducted at 180 °C for different times. The products were collected by filtration, washed with deionized water and ethanol, and finally dried at 60 °C for 6 h. Finally, the dried precipitates were annealed at 400 °C under air for 3 h to obtain the hierarchical porous $NiCo_2O_4$ nanosheets.

Characterizations

The surface morphology of the products were characterized by field emission scanning electron microscope (SEM, FEI, Quanta 400). Transmission electron microscope (TEM, JEM-2010HR), high-resolution TEM (HRTEM, 200 kV), and electron diffraction (ED) were also utilized to characterize the microstructures of the products. The obtained products were also analyzed by X-ray diffraction (XRD, Bruker, D8 Advance) to determine the crystal structures. X-ray energy dispersive spectroscopy (EDS), X-ray photoelectron spectroscopy (XPS, ESCALAB 250), and Laser micro-Raman spectrometry (Renishaw inVia) were applied to study the chemical compositions of the products. BET analyses were performed on a Micromeritics ASAP 2020M accelerated surface area and porosimetry analyzer. The magnetic properties were studied by measuring hysteresis loops at low (5 K) and room temperature (300 K) using a Quantum Design MPMS-XL7 superconducting quantum interference device (SQUID) and a vibrating sample magnetometer (VSM) from Oxford Instruments, respectively.

Electrochemical measurement

The electrochemical measurements were conducted on a PINE instrument in a three-electrode cell by using a reversible hydrogen electrode (RHE) as the reference electrode and a platinum foil as the counter electrode. The working electrode was a glass carbon rotating disk with the diameter of 5 mm. The $NiCo_2O_4$ sample (10.0 mg) was added into 1.9 mL ethanol and 0.1 mL Nafion solution (5 wt%, DuPont, USA) and ultrasonicated for 30 min to obtain a well-dispersed ink. The ink was quantitatively transferred onto the surface of the glass carbon electrode and dried under infrared lamp to obtain an electrocatalyst thin film. The total electrocatalyst loadings were 1.2 mg cm^{-2}. The electrochemical tests were performed in oxygen saturated 0.1 mol L^{-1} KOH solution at room temperature at a sweep rate of 5 mV s^{-1} under a rotating speed of 1600 rpm.

3. Results and discussion

The as-synthesized $NiCo_2O_4$ samples from different hydrothermal reaction times (3 h, 6 h, 9 h and 12 h) are shown in Fig. 1. Fig. 1a and 1b show representative SEM images of the $NiCo_2O_4$ sample with a hydrothermal reaction time of 3 h.

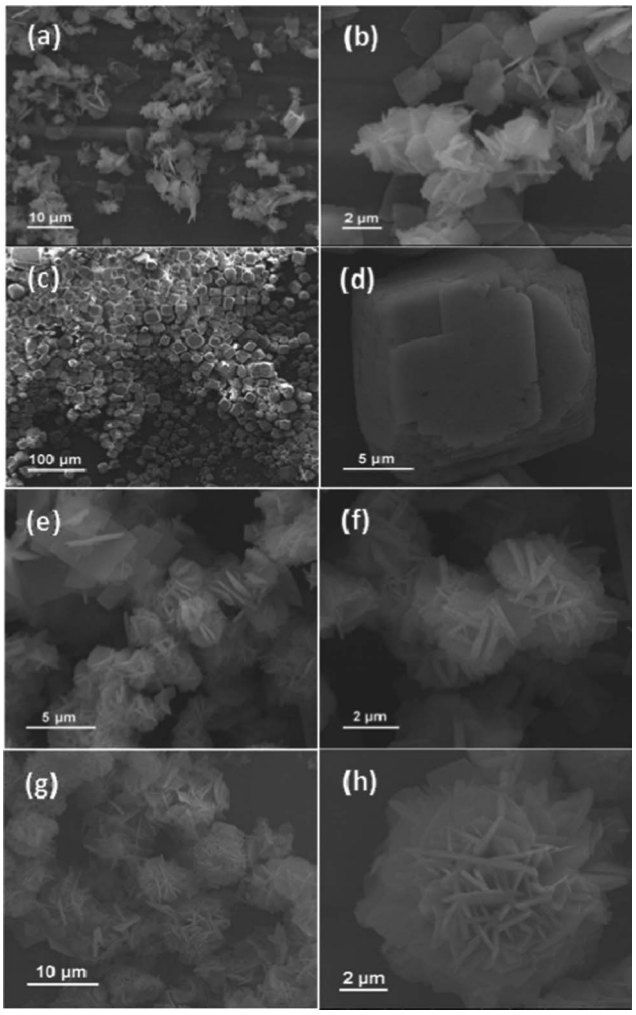

Fig. 1 SEM images of the synthesized $NiCo_2O_4$ samples from different hydrothermal reaction times: (a–b) 3 h; (c–d) 6 h; (e–f) 9 h; (g–h) 12 h.

Obviously, the resulting product is composed of $NiCo_2O_4$ nanosheets. It can be seen that the observed $NiCo_2O_4$ nanosheets have a length of 5–6 μm and width of 3–4 μm, and the thickness is in the range of 100–200 nm. When the hydrothermal reaction time is increased from 3 to 6 h, another hierarchical cubic microstructure consisting of $NiCo_2O_4$ nanosheets with uniform size has been obtained as shown in Fig. 1c and 1d. When the hydrothermal reaction time is 9 h, as shown in Fig. 1e and 1f, $NiCo_2O_4$ hierarchical flower-like super-structures are formed. Such super-structures consist of porous $NiCo_2O_4$ nanosheets. With an increase of hydrothermal reaction time to 12 h, the obtained $NiCo_2O_4$ samples have similar hierarchical flower-like super-structures (Fig. 1g and 1 h) as that of 9 h samples. After calcination at 400 °C for 3 h, the cobalt and nickel metallic carbonate hydroxide salts were decomposed into the $NiCo_2O_4$ phase with the molar ratio of Co : Ni = 2 : 1. The phases of the $NiCo_2O_4$ samples were identified by XRD, and the typical XRD patterns are presented in Fig. 2. Evidently, all the diffraction peaks can be readily assigned to the cubic spinel of $NiCo_2O_4$ (JCPDF card: 20-0781) with lattice constants $a = b = c = 8.11$ Å. The high and sharp peaks indicate that the $NiCo_2O_4$ samples are well crystallized. The results demonstrate that the simple thermal decomposition method is suitable for preparing multiple transition metal oxide nanomaterials, in which the molar ratios of transition metal elements can be easily adjusted.[22,23]

In order to further understand the composition and structure of these $NiCo_2O_4$ samples, Raman analysis was performed and the typical Raman spectrum of the products is shown in Fig. 3. With respect to the as-prepared $NiCo_2O_4$ samples, the peaks at 187, 477.8, 523.5, and 671.2 cm^{-1} correspond to F_{2g}, E_g, F_{2g}, and A_{1g} models of $NiCo_2O_4$, respectively. Only the Co–O and Ni–O vibrations of $NiCo_2O_4$ samples are detected, no signal corresponding to an OH group is observed, indicating the cobalt and nickel metallic carbonate hydroxide salts are completely decomposed after calcinating at 400 °C . These results are consistent with those documented in previous reports.[24,25]

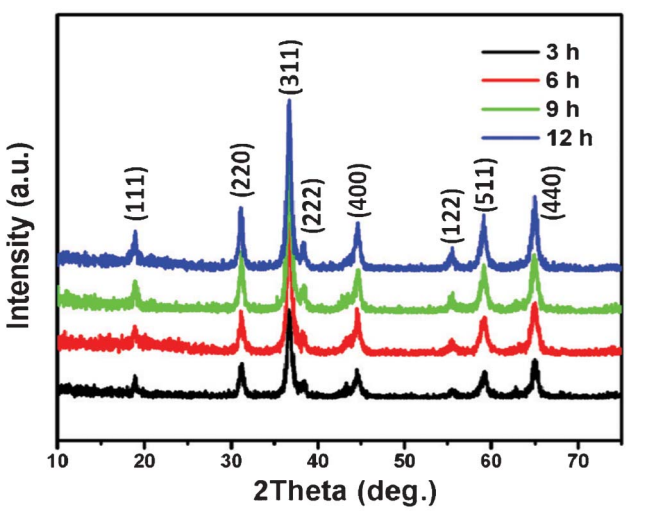

Fig. 2 XRD patterns of $NiCo_2O_4$ samples at 180 °C from different hydrothermal reaction times.

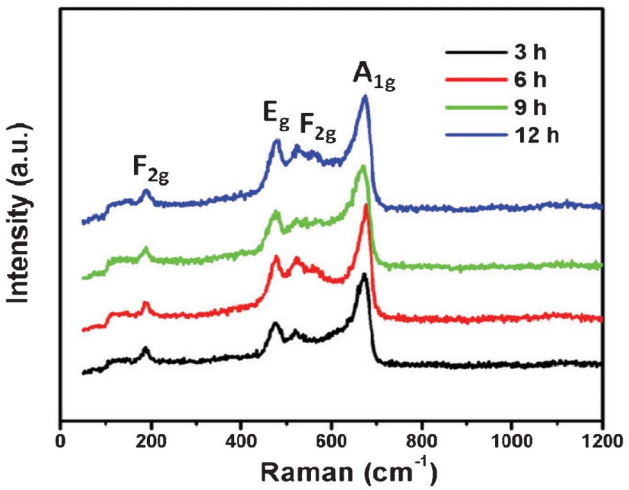

Fig. 3 Room temperature Raman spectra of $NiCo_2O_4$ samples at 180 °C from different hydrothermal reaction times.

TEM measurements were further carried out to analyze the micro- and nanostructures of $NiCo_2O_4$ nanosheets. Fig. 4(a–d)

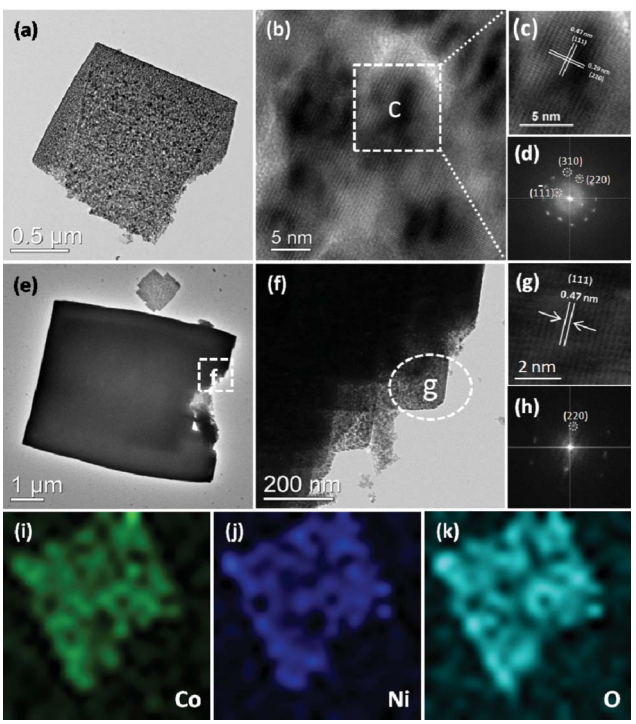

Fig. 4 (a–d) TEM, HRTEM images and SAED pattern of $NiCo_2O_4$ nanosheets obtained from a hydrothermal reaction time of 3 h; (e–h) TEM, HRTEM images and SAED pattern of $NiCo_2O_4$ hierarchical cubic microstructures consisting of $NiCo_2O_4$ nanosheets obtained from a hydrothermal reaction time of 6 h; and (i–k) The corresponding EDX elemental mapping images of $NiCo_2O_4$ nanosheets obtained from a hydrothermal reaction time of 3 h.

show TEM images of an individual $NiCo_2O_4$ nanosheet. The lattice fringes are clearly displayed in the HRTEM image (Fig. 4b), indicating that the $NiCo_2O_4$ nanosheet is of high crystallinity. In addition, the lattice fringes with a *d*-spacing of 0.47 and 0.29 nm can be well indexed to the (111) and (220) planes of cubic $NiCo_2O_4$, respectively. The corresponding selected-area electron diffraction (SAED) pattern shown in Fig. 4d also reflects the crystalline feature of the nanosheet. The TEM, HRTEM images and SAED pattern of $NiCo_2O_4$ hierarchical cubic microstructures consisting of $NiCo_2O_4$ nanosheets are shown in Fig. 4(e–h). The hierarchical cubic microstructure morphology is clearly displayed in the TEM images, as shown in Fig. 4f. The HRTEM image and SAED pattern in Fig. 4(g–h) indicate that the hierarchical cubic microstructure of $NiCo_2O_4$ is highly crystalline. The well-resolved one-dimensional lattice fringe with the spacing of 0.47 nm can be indexed to the (111) plane of cubic $NiCo_2O_4$. In order to further elucidate microscopic structure, the TEM-EDX (energy dispersive X-ray) elemental full and line mapping techniques were applied to an individual nanosheet. As shown in Fig. 4(i–k), it can be seen that Co, Ni, and O are distributed as nanosheets. The result further confirms that the as-prepared samples are composed of $NiCo_2O_4$. As a result, it is concluded that although the $NiCo_2O_4$ nanosheets and nanocubes are of different morphology, they have similar crystallinity characteristics, which implies possible similar performance.

$NiCo_2O_4$ hierarchical flower-like super-structures consisting of porous $NiCo_2O_4$ nanosheets are clearly observed in the TEM image as shown in Fig. 5a. As we all known, the porous structure will greatly improve the surface area. The HRTEM image of the $NiCo_2O_4$ hierarchical flower-like super-structure is shown in Fig. 5c, which is recorded from the selected region of Fig. 5b. The lattice fringes with a *d*-spacing of 0.47 and 0.29 nm can be well indexed to the (111) and (220) planes of the $NiCo_2O_4$ hierarchical flower-like super-structure, respectively, which is the same as the $NiCo_2O_4$ nanosheets as shown in Fig. 4. The angle between (111) and (220) planes is measured to be about 90°, which is in agreement with the calculated value of 90°. Fig. 5d shows the corresponding SAED pattern of $NiCo_2O_4$ hierarchical flower-like super-structure (marked by a white square in Fig. 5a). The reflections corresponding to (111), (220) and (310) planes confirm that the porous $NiCo_2O_4$ hierarchical flower is single crystalline with cubic structure, the result is in accordance with the XRD results. The energy dispersive X-ray spectroscopy (EDS) pattern was also conducted from the square area of the porous $NiCo_2O_4$ hierarchical flower-like super-structure, as shown in Fig. 5e. Besides the Cu peaks coming from the TEM grid, only the elements Ni, Co and O are detected in the EDS spectrum. The composition analysis reveals the stoichiometry Ni : Co : O in the sample is about 1 : 2 : 4, which proves that the whole porous hierarchical flower-like super-structure consists of $NiCo_2O_4$.

To gain further information on the elemental composition of $NiCo_2O_4$ samples, we resorted to X-ray photoelectron spectroscopy (XPS) measurement and the results are shown in Fig. 6(a–c). The elements Ni, Co and O are detected from $NiCo_2O_4$ samples. Fig. 6(a–c) show the multiplex spectra of Ni, Co, and O. The high-resolution spectrum for the O 1s region in Fig. 6a shows two and three oxygen contributions, which have been denoted as O1, O2, and O3. The fitting low energy peak of O1 at 529.6 eV in the O 1s XPS spectrum is typical of the O atoms in the O–Co/Ni bonding structure.[26] The well-resolved component energy peak of O2 at 531.4 eV corresponds to a number of defect sites with low oxygen coordination in the material with small particle size.[27] Furthermore, the compo-

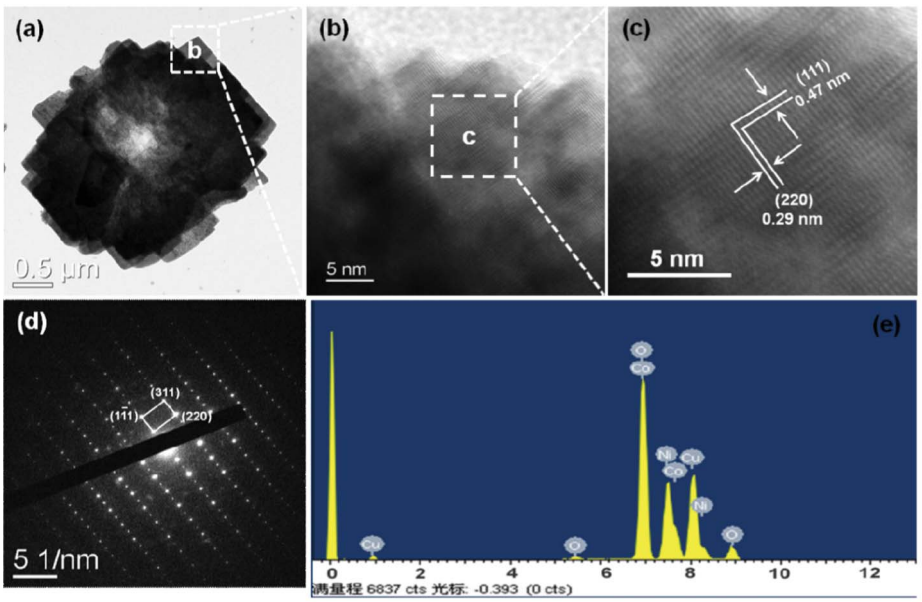

Fig. 5 (a–e) TEM, HRTEM images, SAED pattern and the EDS spectrum of $NiCo_2O_4$ hierarchical flower-like super-structures consisting of porous $NiCo_2O_4$ nanosheets.

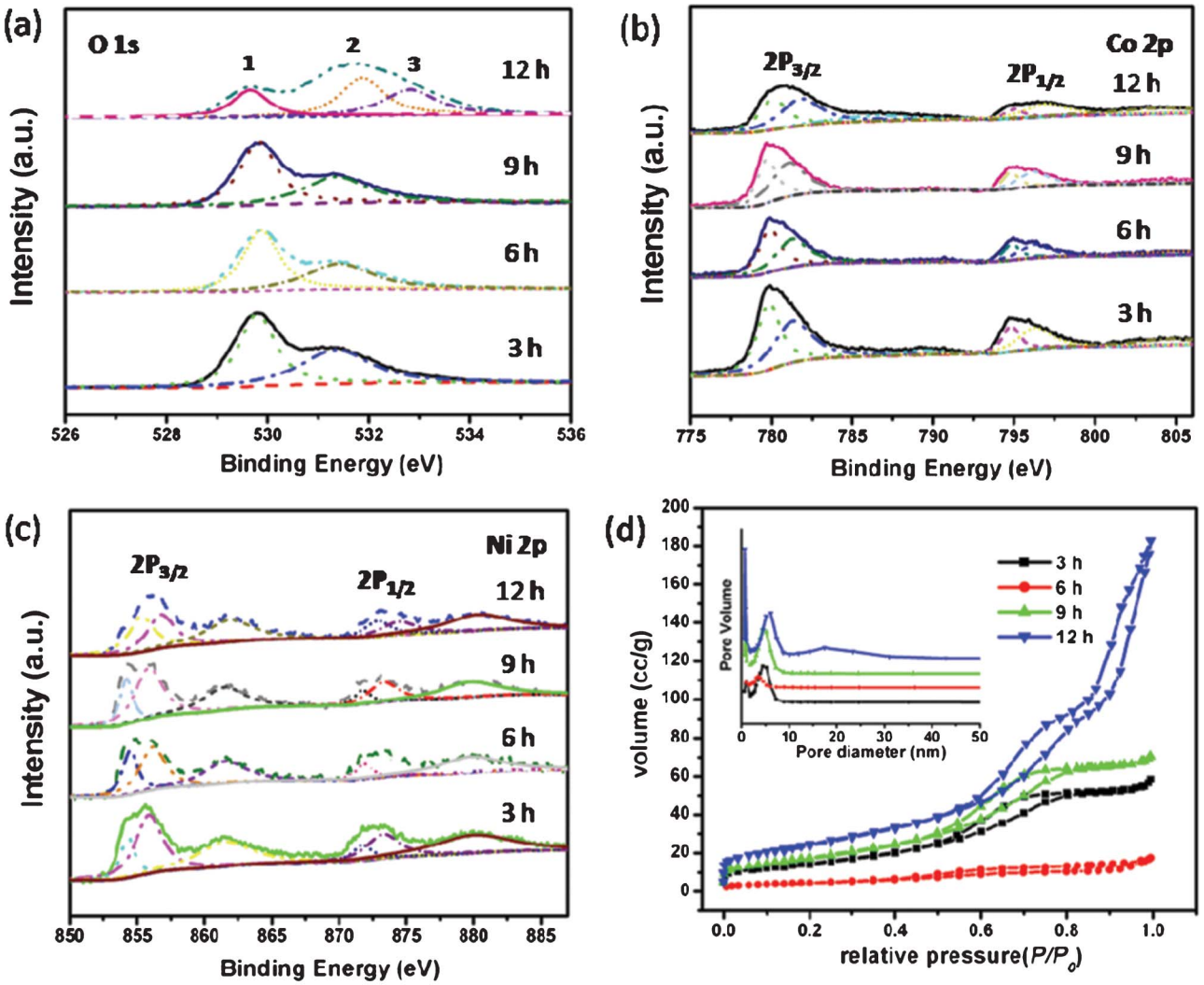

Fig. 6 (a–c) XPS spectra of $NiCo_2O_4$ samples at 180 °C from different hydrothermal reaction times; (d) N_2 adsorption/desorption isotherms of $NiCo_2O_4$ samples with corresponding pore-size distribution (inset).

nent high energy peak of O3 at 532.8 eV can be attributed to the multiplicity of physi- and chemisorbed water at and within the material surface.[28] With regards to the Co 2p XPS spectrum, the binding energy at 779.9 and 795.0 eV for $2p_{3/2}$ and $2p_{1/2}$ transitions are associated with Co^{3+}. The relatively narrow peak width, the $2p_{3/2}$ to $2p_{1/2}$ separation of 15.1 eV, and the absence of shake-up peak all reveal that no Co^{2+} cations exist in $NiCo_2O_4$.[28,29] The Ni 2p XPS spectrum in Fig. 6c has revealed that the main $2p_{3/2}$ peak is at 855.6 eV, which is close to 854.9 eV for Ni^{2+} but much lower than 857.1 eV for Ni^{3+}.[30,31] Moreover, there are two shake-up type peaks of nickel at the high binding energy side of the Ni $2p_{3/2}$ and $2p_{1/2}$ edge. Therefore, we are confident that Ni is in the divalent state.

The precursor metal carbonate hydroxide salts were formed by reacting metal cations with anions slowly released from hydrolysis of urea in an aqueous solution. The metal carbonate hydroxide salts were decomposed into metal oxide by calcination. The relevant chemical reactions involved can be presented as eqn (1)–(3):[32]

$$2Ni^{2+} + CO_3^{2-} + 2OH^- \rightarrow Ni_2CO_3(OH)_2 \quad (1)$$

$$2Co^{2+} + CO_3^{2-} + 2OH^- \rightarrow Co_2CO_3(OH)_2 \quad (2)$$

$$Ni_2CO_3(OH)_2 + 2Co_2CO_3(OH)_2 + O_2 \rightarrow 2NiCo_2O_4 + 3CO_2 + 3H_2O \quad (3)$$

Here, a general growth mechanism for the different morphologies of $NiCo_2O_4$ formation is suggested, based on the previous analytical results. This mechanism consists of three steps. The first step denotes the coprecipitation step. When adding urea solution to the solution of Ni^{2+} and Co^{2+}, the $Ni_2CO_3(OH)_2$ and $Co_2CO_3(OH)_2$ coprecipitate to form precursor particles, as described by reactions (1) and (2). Generally, these particles are thin platelet-like conglomerations.[33,34] This step is followed by the second in which the

Table 1 BET surface areas and pore parameters of $NiCo_2O_4$ samples

$NiCo_2O_4$	BET specific surface area/m^2 g^{-1}	BJH pore volume/mL g^{-1}	BJH average pore size/mL g^{-1}
3 h	53.27	0.09	5.09
6 h	16.34	0.03	5.23
9 h	64.17	0.11	4.99
12 h	88.85	0.28	9.68

coprecipitates are heated to approximately 180 °C under hydrothermal reaction for different times. The different morphologies of precursors are obtained by the particles' rearrangement. The third step is a reaction of $Ni_2CO_3(OH)_2$ and $Co_2CO_3(OH)_2$ with O_2 to form the $NiCo_2O_4$ spinel phase by calcination under 400 °C for 3 h, with CO_2 and gaseous H_2O release, as described by reaction (3).

The porous characteristics of $NiCo_2O_4$ samples were further investigated by nitrogen adsorption and desorption measurement at 77 K. The specific surface areas, pore volumes, and the corresponding Barrett–Joyner–Halenda (BJH) pore size distribution plots are presented in Fig. 6d and Table 1. All of the adsorption isotherms can be categorized as type IV with a Type H1 hysteresis loop, revealing a narrow distribution of pore size.[32,35] The specific surface areas of $NiCo_2O_4$ samples are 53.27, 16.34, 64.17, and 88.85 m^2 g^{-1}, respectively, which are presented in Table 1. The BET results are in agreement with the TEM observations discussed above, showing a porous structure with relatively high surface area. These structural characteristics have implications for applications in the electrochemical and magnetic fields, which comes as following below.[36]

The ORR reduction reaction (ORR) activity of the $NiCo_2O_4$ samples was measured in an oxygen-saturated 0.1 mol L^{-1} KOH solution with the rotation speed of the electrode at 1600 rpm and a potential sweep rate of 5 mV s^{-1} at room temperature, as shown in Fig. 7. It is a meaningful finding that the prepared $NiCo_2O_4$ sample shows ORR activity. As is well know the ORR is usually catalyzed by noble metals which cause the high cost of fuel cells, the research community has been endeavouring to replace the noble metal catalyst with non-noble metals. The oxide prepared in this study shows meaningful potential for application in ORR for fuel cells. The $NiCo_2O_4$ hierarchical flower-like super-structures consisting of porous $NiCo_2O_4$ nanosheets will bring high active surface area and provide fast transport for the electroactive species from the solution to the reaction site. The $NiCo_2O_4$ nanosheets exhibit an ORR onset potential between 0.70 and 0.86 V, and the overpotential is relatively high for the hierarchical cubic microstructure compared with the nanosheets under the same conditions, as shown in Fig. 7a. After 1000 cycles, the half-wave potentials of $NiCo_2O_4$ samples remain nearly unchanged in Fig. 7b, which proves the superior cycling stabilities of the $NiCo_2O_4$ samples in ORR. The results suggest that these $NiCo_2O_4$ samples are promising candidates for building high performance ORR catalysts with superior stability.

The magnetic properties of the $NiCo_2O_4$ samples were also investigated. The typical magnetization hysteresis loops for $NiCo_2O_4$ samples at 5 K are shown in Fig. 8a. The nonlinear curves with nonzero remnant magnetization and coercivity show well-pronounced hard magnetic property. The coercivity field (H_c) of the $NiCo_2O_4$ nanosheets is 258.8 Oe, and the corresponding remanent magnetization (M_r) is 0.08 emu g^{-1}. With increasing hydrothermal reaction time, the obtained $NiCo_2O_4$ samples show higher H_c and M_r than the $NiCo_2O_4$ nanosheets as shown in Fig. 8a. Especially, the $NiCo_2O_4$ hierarchical flower-like super-structures consisting of porous $NiCo_2O_4$ nanosheets exhibit superior H_c and M_r, which are 1667.4 Oe and 0.23 emu g^{-1}, respectively. Due to their different nanostructures, H_c is likely to have two main factors apart from magneto-crystalline anisotropy: shape anisotropy and the interface ferromagnetic–antiferromagnetic exchange coupling, where the ferromagnetic is origin from the defects of interfaces. As the material transforms from nanosheets to hierarchical flower-like super-structures, its shape anisotropy increases significantly, leading to an increase in coercivity.[37]

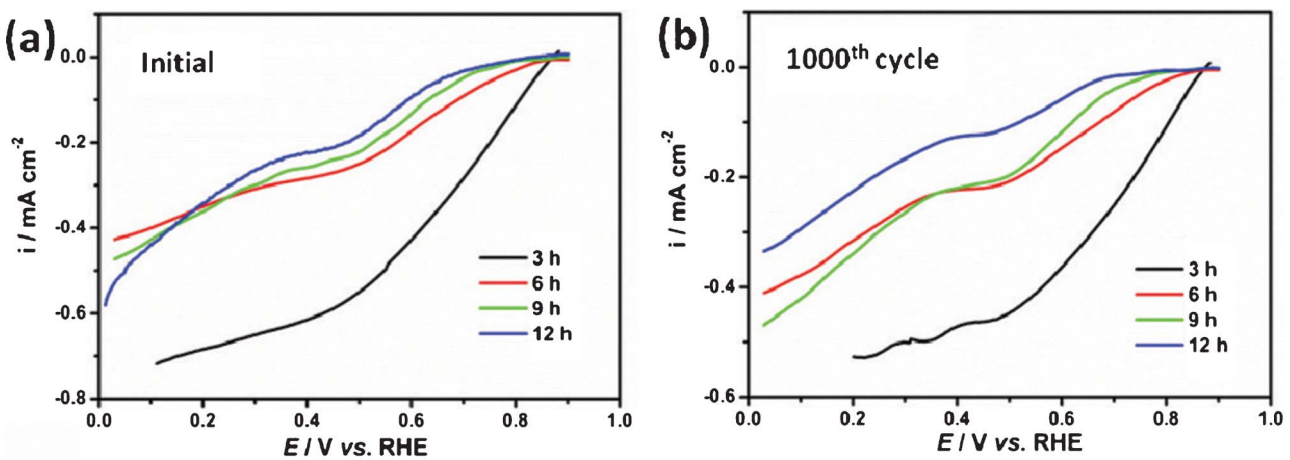

Fig. 7 (a) Linear potential sweep curves for the ORR on $NiCo_2O_4$ samples; (b) ORR curves after 1000 cycles on $NiCo_2O_4$ samples.

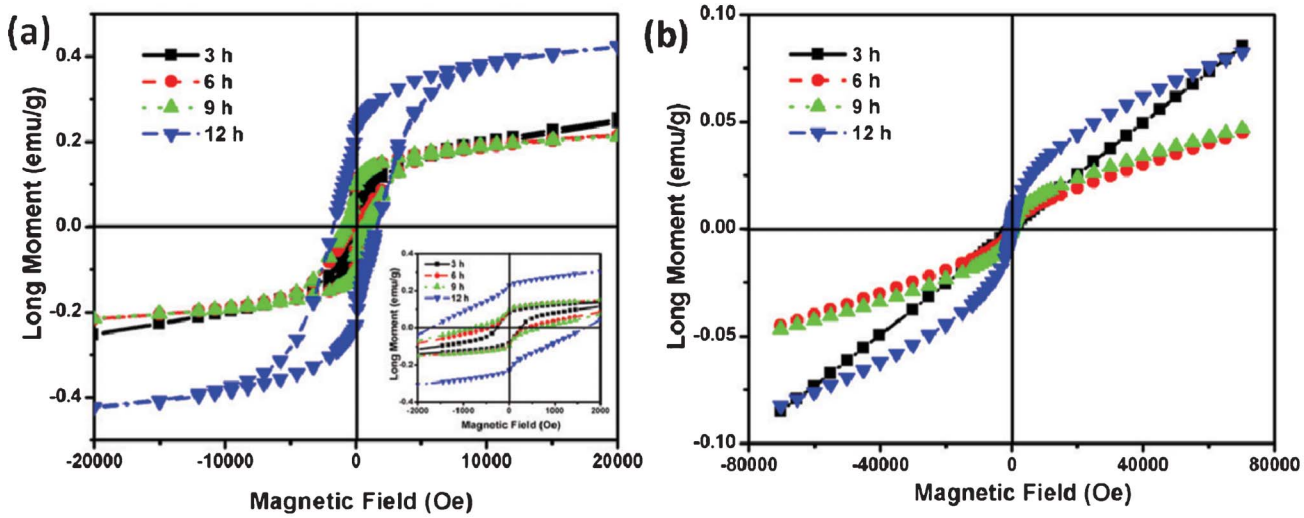

Fig. 8 (a) Low temperature 5 K hysteresis loops of $NiCo_2O_4$ samples and an enlarged view at low field is shown in the inset. (b) Room temperature hysteresis loops of $NiCo_2O_4$ samples.

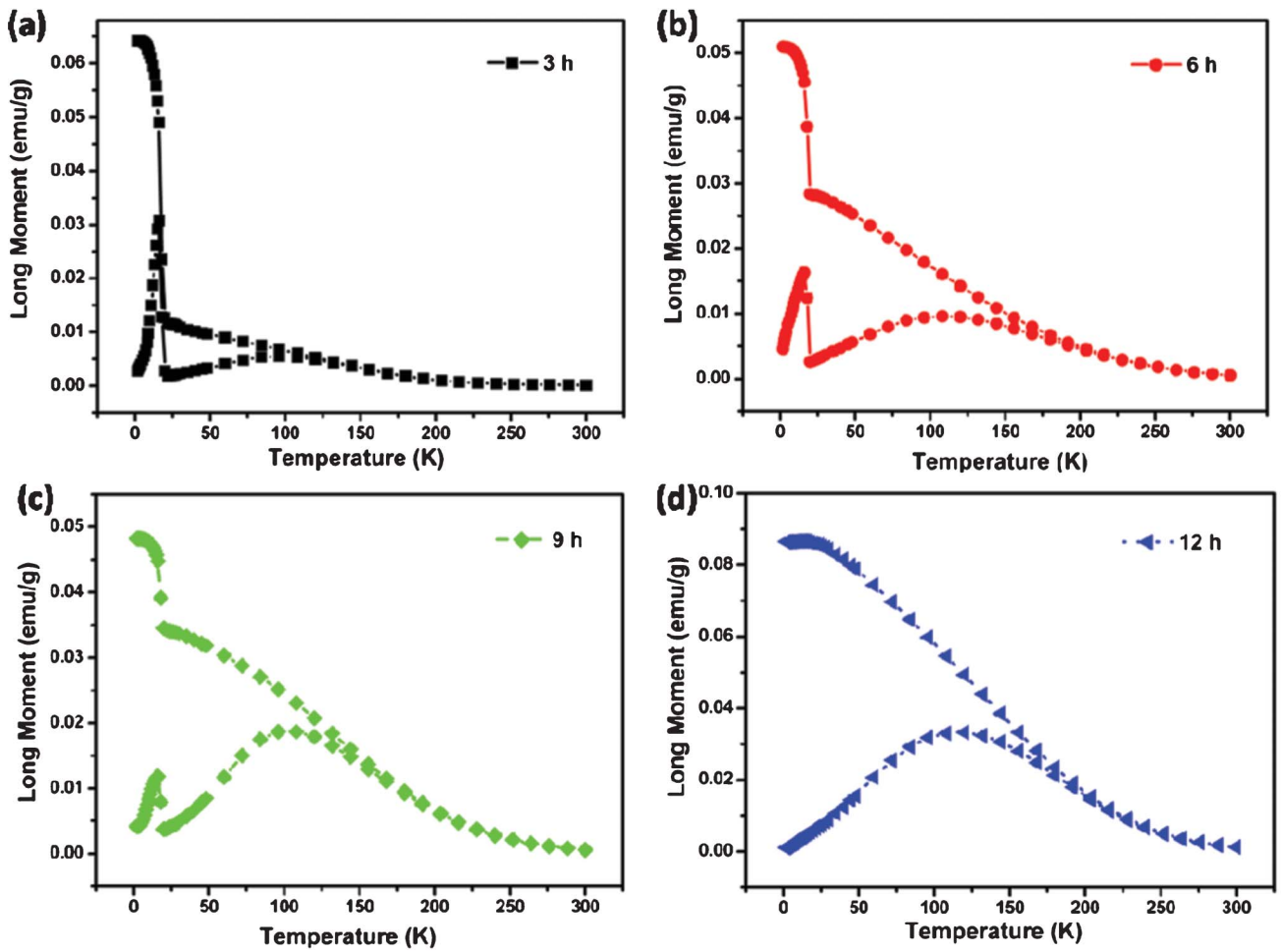

Fig. 9 (a–d) ZFC-FC curves of $NiCo_2O_4$ samples at 100 Oe.

Fig. 8b represents the field-dependent magnetic behavior of the as-prepared $NiCo_2O_4$ samples, measured at room temperature (300 K). However, the hysteresis loop of the as-prepared $NiCo_2O_4$ samples does not reach saturation, even for the applied magnetic field 7 kOe, and no finite coercive field is observed, indicating the as-prepared $NiCo_2O_4$ samples are typical of soft magnetic behavior at room temperature.[38,39]

The zero field cooled (ZFC) and field cooled (FC) magnetization data for the as-prepared $NiCo_2O_4$ samples, measured at 100 Oe, are shown in Fig. 9. The samples were cooled from room temperature to 5 K, without any external magnetic field (ZFC), and the magnetization was recorded while warming the samples in an applied uniform external field of 100 Oe. As expected, the magnetization is seen to initially increase upon warming and then to decrease after reaching a maximum value. The temperature at which the maximum is observed is called the Neel temperature (T_N), and the point where the ZFC and FC magnetization curves bifurcate is defined as irreversible temperature (T_{irr}). When the same samples were cooled under a magnetic field (FC) of 100 Oe, the magnetization behavior differs significantly from that of ZFC measurements, and the two together reveal information about the magnetic state of the samples. The bifurcation of ZFC and FC magnetization starts above T_N and grows below it. The strong irreversibility at low temperatures between the ZFC and FC curves is due to the existence and distribution of the energy barriers of the magnetic anisotropy and the slow relaxation of particles below the Neel temperature.[40] In addition, large irreversibility also indicates an induced preferential orientation of the particle moments along the applied field. Especially, the ZFC-FC curves of all the samples except that the 12 h sample seem to show an unexpected trend at low temperature, both the ZFC and the FC curves drop significantly at 15 K. Notably, the magnetic order transition have a ''freezing'' of surface spins, which can be attributed to the defects in the surface of nanosheets. When the temperature is low enough, these spins are ''freezing'' and exhibit ferromagnetic properties. Furthermore, ferromagnetic–antiferromagnetic exchange coupling obviously improves the magnetization, and the spins turn out to be disorder at high temperature and lead to the decrease of magnetization.

4. Conclusions

In summary, we have successfully prepared a novel hierarchical flower-like super-structures consisting of porous $NiCo_2O_4$ nanosheets *via* a simple and controlled hydrothermal method. The electrochemical results suggest that these $NiCo_2O_4$ samples are promising candidates for ORR catalysts with high performance and stability. Furthermore, the magnetic measurement of $NiCo_2O_4$ samples shows the strong irreversibility at ZFC and FC curves. These $NiCo_2O_4$ materials are potentially important for application in supercapacitors, lithium-ion battery electrode materials and catalysts. Moreover, the fabrication and inherent characteristic of $NiCo_2O_4$ nanostructures may open up the prospect of synthesizing and understanding other transition-metal oxide multifunctional materials.

Acknowledgements

This work was supported by Natural Science Foundations of China (Grant No. 21203036), the Natural Science Foundations of Guangdong Province (Grant No. s2011040004152), and the Innovative Talents Cultivation Project of Guangdong Province (Grant No. LYM11096) and the Science and Technology Project of Guangzhou (Grant No. 12C52011624 and 12C72011619).

References

1 J. S. Son, J. H. Yu, S. G. Kwon, J. Lee, J. Joo and T. Hyeon, *Adv. Mater.*, 2011, **23**, 3214–3219.
2 J. Liu and X. W. Liu, *Adv. Mater.*, 2012, **24**, 4097–4111.
3 L. Zhang, Q. Zhang and J. Li, *Adv. Funct. Mater.*, 2007, **17**, 1958–1965.
4 C. Zhi, Y. Bando, C. Tang, H. Kuwahara and D. Golberg, *Adv. Mater.*, 2009, **21**, 2889–2893.
5 K. H. Park, K. Jang and S. U. Son, *Angew. Chem., Int. Ed.*, 2006, **45**, 4608–4612.
6 C. Wang, Y. Zhou, M. Ge, X. Xu, Z. i Zhang and J. Z. Jiang, *J. Am. Chem. Soc.*, 2010, **132**, 46–47.
7 X. Yu, J. Yu, B. Cheng and M. Jaroniec, *J. Phys. Chem. C*, 2009, **113**, 17527–17535.
8 G. R. Li, C. Z. Yao, X.-H. Lu, F. L. Zheng, Z. P. Feng, X. L. Yu, C. Y. Su and Y. X. Tong, *Chem. Mater.*, 2008, **20**, 3306–3314.
9 B. Liu, J. Zhang, X. Wang, G. Chen, D. Chen, C. Zhou and G. Shen, *Nano Lett.*, 2012, **12**, 3005–3011.
10 C. F. Windisch Jr, G. J. Exarhos, K. F. Ferris, M. H. Engelhard and D. C. Stewart, *Thin Solid Films*, 2001, **398**, 45–52.
11 Q. A. Pankhurst, J. Connolly, S. K. Jones and J. Dobson, *J. Phys. D: Appl. Phys.*, 2003, **36**, R167–R181.
12 B. Cui, H. Lin, J. B. Li, X. Li, J. Yang and J. Tao, *Adv. Funct. Mater.*, 2008, **18**, 1440–1447.
13 S. N. Kale, A. D. Jadhav, S. Verma, S. J. Koppikar, R. Kaul-Ghanekar, S. D. Dhole and S. B. Ogale, *Nanomed.: Nanotechnol., Biol. Med.*, 2012, **8**, 452–459.
14 L. Hu, L. Wu, M. Liao and X. Fang, *Adv. Mater.*, 2011, **23**, 1988–1992.
15 Q. Li, L. Zeng, J. Wang, D. Tang, B. Liu, G. Chen and M. Wei, *ACS Appl. Mater. Interfaces*, 2011, **3**, 1366–1373.
16 B. Cui, H. Lin, Y. Z. Liu, J. B. Li, P. Sun, X. C. Zhao and C. J. Liu, *J. Phys. Chem. C*, 2009, **113**, 14083–14087.
17 M. Cabo, E. Pellicer, E. Rossinyol, O. Castell, S. Suriñach and M. D. Baró, *Cryst. Growth Des.*, 2009, **9**, 4814–4821.
18 C. Z. Yuan, J. Y. Li, L. R. Hou, X. G. Zhang, L. F. Shen and X. W. Lou, *Adv. Funct. Mater.*, 2012, **22**, 4592–4597.
19 S. Verma, H. M. Joshi, T. Jagadale, A. Chawla, R. Chandra and S. Ogale, *J. Phys. Chem. C*, 2008, **112**, 15106–15112.
20 G. Zhang, H. B. Wu, H. E. Hoster, M. B. Chan-Park and X. W. Lou, *Energy Environ. Sci.*, 2012, **5**, 9453–9456.
21 H. Jiang, J. Ma and C. Li, *Chem. Commun.*, 2012, **48**, 4465–4467.

22 Y. Li, P. Hasin and Y. Wu, *Adv. Mater.*, 2010, **22**, 1926–1929.
23 J. Chang, J. Sun, C. Xu, H. Xu and L. Gao, *Nanoscale*, 2012, **4**, 6786–6791.
24 Z. A. Hu, Y. L. Xie, Y. X. Wang, L. J. Xie, G. R. Fu, X. Q. Jin, Z. Y. Zhang, Y. Y. Yang and H. Y Wu, *J. Phys. Chem. C*, 2009, **113**, 12502–12508.
25 J. H. Zhong, Z. L. Wang, G. R. Li, J. W. Wang, Y. N. Ou and Y. X. Tong, *J. Mater. Chem.*, 2012, **22**, 5656–5665.
26 J. Xiao and S. Yang, *J. Mater. Chem.*, 2012, **22**, 12253–12262.
27 C. Yuan, J. Li, L. Hou, L. Yang, L. Shen and X. Zhang, *J. Mater. Chem.*, 2012, **22**, 16084–16090.
28 J. G. Kim, D. L. Pugmire, D. Battaglia and M. A. Langell, *Appl. Surf. Sci.*, 2000, **165**, 70–84.
29 Y. E. Roginskaya, O. V. Morozova, E. N. Lubnin, Y. E. Ulitina, G. V. Lopukhova and S. Trasatti, *Langmuir*, 1997, **13**, 4621–4627.
30 M. W. Nydegger, G. Couderc and M. A. Langell, *Appl. Surf. Sci.*, 1999, **147**, 58–66.
31 M. Oku and K. Hirokawa, *J. Solid State Chem.*, 1979, **30**, 45–53.
32 J. Xiao and S. Yang, *RSC Adv.*, 2011, **1**, 588–595.
33 B. Salvadori and L. Dei, *Langmuir*, 2001, **17**, 2371–2374.
34 H. Cai, A. C. Hillier, K. R. Franklin, C. C. Nunn and M. D. Ward, *Science*, 1994, **266**, 1551–1555.
35 K. S. W. Sing, D. H. Everett, R. A. W. Haul, L. Moscou, R. A. Pierotti, J. Rouquerol and T. Siemieniewska, *Pure Appl. Chem.*, 1985, **57**, 603–619.
36 J. Roggenbuck and M. Tiemann, *J. Am. Chem. Soc.*, 2005, **127**, 1096–1097.
37 M. Cabo, E. Pellicer, E. Rossinyol, M. Estrader, A. López-Ortega, J. Nogués, O. Castell, S. Suriñach and M. D. Baró, *J. Mater. Chem.*, 2010, **20**, 7021–7028.
38 S. Verma and P. A. Joy, *J. Appl. Phys.*, 2005, **98**, 124312.
39 Z. X. Tang, C. M. Sorensen, K. J. Klabunde and G. C. Hadjipanayis, *Phys. Rev. Lett.*, 1991, **67**, 3602–3605.
40 A. J. Rondinone, A. C. S. Samia and Z. J. Zhang, *J. Phys. Chem. B*, 1999, **103**, 6876–12508.

